Fast Analytical Solver for Fuel-Optimal Speed Trajectory of Connected and/or Automated Vehicles

Jihun Han and Jackeline Rios-Torres, *Senior Member, IEEE*

Abstract— A longitudinal fuel-optimal speed trajectory has been found to be a control sequence of four possible modes: maximum acceleration, constant speed cruising, coasting, and maximum braking. However, a numerical optimization solver is required, which has been shown to have a tradeoff between computing efficiency and optimality. This article presents a fast analytical solver that computes the longitudinal fuel-optimal speed trajectory for connected and automated vehicles (CAVs). We formulate a longitudinal fuel-optimal control problem and transform it into a boundary value problem (BVP) through Pontryagin's minimum principle. By analyzing the costate dynamics of the BVP, we investigate the underlying mechanism required to build the control sequences that consist of multiple modes for a given boundary condition (BC). This approach allows us to identify feasible control sequences and establish feasible criteria for BC for each sequence. Unlike BVP numerical solvers that require a good initial guess, initial costates can be analytically obtained by linking each mode that has an explicit solution after the control sequence is specified by BC. Finally, we show that CAVs equipped with the proposed solver lead to significant fuel savings for single and multiple-vehicle scenarios with different CAV penetration rates.

Index Terms— Analytical optimization solver, connected and automated vehicles (CAVs), fuel-optimal control, Pontryagin's minimum principle.

I. Introduction

OVER the past decade, advanced technologies on connectivity and automation functions have been developed and are integrated into new vehicles. Such technologies provide

control researchers and engineers an unprecedented opportunity to improve safety, increase fuel/energy benefits, and improve/resolve traffic congestion [1], [2], [3]. An adaptive cruise control (ACC) is an automation function for road vehicles that use sensor information about the surrounding environment and automatically adjusts the vehicle speed to maintain a safe distance gap with the preceding vehicle. In the beginning, a design of ACC systems considered safety, i.e., crash avoidance, as a main criterion, but recently, fuel/energy savings have become an additional design criterion. This new approach to the design of ACC systems is known as ecological ACC [4], [5]. Furthermore, cooperative ACC (CACC) and ecological CACC systems [6], [7] are being subject of research due to vehicle-to-everything (V2X) connectivity. According to [8], many studies about the ecological ACC have shown significant energy-saving potentials in various scenarios, e.g., highway driving, arterial driving on signalized/nonsignalized intersections, and merging onto a highway. Some studies implemented and validated online controllers under real-world driving situations.

To harness the full energy-saving potential, there are several model-based optimization methods: 1) dynamic programming (DP); 2) a direct method; and 3) an indirect method according to [9]. The DP is a well-known method that easily addresses complex optimal control problems (OCPs) while guaranteeing the global optimality based on the principle of optimality [10]. However, it has a tradeoff between computing efficiency and optimality [11]. It can be generally considered as a benchmark computed offline, but not as a real-time implementable optimization algorithm. To overcome this drawback, some studies approximated the OCP and solved it to meet requirements for real-time implementation [12], [13], [14], whereas other studies used high-performance computing systems and updated the solution through a cloud server [15], [16].

The direct method is widely used for model predictive control (MPC). It discretizes and converts the OCP into a constrained nonlinear optimization problem. Depending on the OCP formulation, including cost, system models, and constraints, the complexity to get the solution differs. Nonlinearity involving aerodynamic drag resistance in a longitudinal vehicle dynamic model and a nonconvex cost function make the OCP more difficult to solve to properly find an optimal solution. Linearization and convexification are often applied to modify the OCP and enable the MPC implementation of ACC [4], [5] and platooning control [17], [18], [19]. The vehicle platooning enables a group of vehicles to travel close to each other at a high speed, so it saves energy by improving aerodynamic efficiency while increasing traffic capacity in a traffic network.

The MPC is generally executed for a short prediction horizon up to a few seconds because of the required discretization. An alternative approach to solving the MPC involves converting the original OCP into a mixed integer linear programming problem that includes discrete decisions [20], [21].

The indirect method provides an optimal control policy through the application of the Pontryagin minimum principle (PMP) [22], helping to understand the theoretical mechanisms under eco-driving [23], [24]. The optimal control policy differs depending on the OCP formulation [25]; for example, the optimal policy for internal combustion engine vehicles (ICEVs) includes several modes, including maximum acceleration, maximum braking, coasting with engine shutdown, and constant speed cruising, to maximize fuel savings. A similar conclusion was reached in [26] by using other numerical optimization methods. Using the resulting optimal control policy, the OCP is transformed into a boundary value problem (BVP) that must satisfy boundary conditions (BCs). Nonlinearity and nonconvexity are still the main hurdles in solving a BVP, so a numerical method (e.g., shooting and collocation) is required [27]. The numerical method has been improved to achieve faster convergence and fewer iterations, resulting in a more computing-efficient and accurate BVP solution [28], [29]. To facilitate the BVP treatment, the OCP was simplified [30], [31], and the simplification led to derive a closed-form BVP solutions that are suitable for real-time implementation [32], [33], [34], [35]. On the other hand, some studies combined the optimal control policy with either the direct method or DP to generate vehicle state trajectories [36], [37]. Furthermore, important insights extracted from the optimal control policy were included in generating trajectories, i.e., a pulse-and-glide strategy (maximum acceleration and coasting) is beneficial for ICEVs to save more fuel [38], [39].

Three key considerations drove the development of the BVP solver proposed in this article for a fuel-optimal driving control: 1) fuel optimality; 2) computational efficiency; and 3) robustness. To this end, we developed a fast analytical BVP solver to compute the fuel-optimal speed trajectory. This article focuses on the underlying theory and algorithm of the proposed solver. We consider the nonlinear longitudinal vehicle dynamic model and identify feasible control sequences by analyzing the BVP costate dynamics based on the indirect method in order to achieve near fuel optimality. Then, we use explicit solutions for each interval to establish the relationship between feasible control sequences and BCs, which enables the control sequence selection using BC without the initial guess required to solve the BVP numerically; this method can significantly reduce computing time while increasing the robustness. Finally, as a case study for deeper understanding of the proposed solver, we present a systematic sensitivity analysis for single-vehicle scenarios and show fuel saving potentials for multiple-vehicle scenarios with different penetration rates (PRs) of connected and automated vehicles (CAVs). Note that we provided analytical insights into eco-driving using this solver in [23] and showed application results for on-ramp merging scenarios in [40], but none of these provided the solver algorithm details.

TABLE I
SYSTEM MODEL PARAMETERS

Coefficient	Value	Unit	Coefficient	Value	Unit
m	1100	kg	q_2	-7.415×10^{-4}	ml·s/m^2
ρ_a	1.184	kg/m^3	q_3	5.975×10^{-5}	ml·s^2/m^3
A_f	2.13	m^2	r_0	0.07224	ml·s/m
c_d	0.33	-	r_1	9.681×10^{-2}	ml·s^2/m^2
c_r	0.015	-	r_2	1.075×10^{-3}	ml·s^3/m^3
g	9.81	m/s^2	p_0	0.1569	ml/s
q_0	0.1569	ml/s	p_1	0.1249	ml·s^2/m^2
q_1	2.45×10^{-2}	ml/m	p_2	0.0409	ml/m

This article is organized as follows. Section II includes the formulation of the fuel-optimal speed control problem. Section III shows the derivation of the analytical fuel-optimal solutions and identifies their relationship with the BCs. Section IV presents the results of a simulation study using the proposed solver. Finally, conclusions and future work are discussed in Section V.

II. FUEL-OPTIMAL SPEED CONTROL PROBLEM

A. Vehicle Longitudinal Dynamics

The following vehicle model is considered:

$$\dot{s} = v \tag{1}$$
$$\dot{v} = \left(F_t - F_b - \left(F_a + F_{rr} + F_g\right)\right)/m$$
$$= a_t - a_b - \frac{\rho_a c_d A_f v^2}{2m} - c_r g \cos\alpha(s) - g \sin\alpha(s) \tag{2}$$

where $a_t = F_t/m$ and $a_b = F_b/m$ (≥ 0), while F_t is the traction force at the wheels and F_b is the mechanical braking force. The aerodynamic drag resistance F_a, the rolling resistance F_{rr}, and the hill climbing resistance F_g are the resistive forces. The state variables, s and v, are the vehicle's position and speed, respectively. The parameter m is the vehicle mass, ρ_a is the external air density, A_f is the vehicle frontal area, c_d is the aerodynamic drag coefficient, c_r is the rolling resistance coefficient, g is the gravity acceleration, and α is the road slope as a function of the position. A vehicle specification is given in Table I.

B. Fuel Consumption Model

In this article, we considered ICEVs, which are propelled by an engine connected to a transmission. Assuming no slip at the wheels, the required traction force and vehicle speed through the transmission from the engine are expressed as

$$F_t = T_e \eta_t^{\text{sign}(T_e)} R_t/r \tag{3}$$
$$v = w_e r/R_t \tag{4}$$

where T_e and w_e are the engine torque and speed, respectively, R_t is the transmission ratio, η_t is the transmission efficiency, and r is the wheel radius. The fuel injection rate is directly related to engine torque and speed. For this reason, a static engine fuel rate map is tabulated as a function of engine torque and speed and used to compute fuel consumption. However, given a desired acceleration at a certain speed, the operation point depends on the gear ratio selected by a gear shift strategy. Assuming the best gear shift strategy that operates the engine in the most efficient way as in [41], the engine

map, $\dot{m}_f(\omega_e, T_e)$, can be converted to a polynomial function of the desired acceleration and speed, $\dot{m}_f(v, a_t)$, as follows:

$$\dot{m}_f(v, a_t) = \begin{cases} \sum_{i=0}^{3} q_i v^i + a_t \sum_{j=1}^{2} r_j v^j, & a_t > 0 \\ 0, & a_t = 0 \end{cases} \quad (5)$$

where the coefficients, q's and r's, are given in Table I.

C. Speed Limit Constraints

To obey road traffic rules, the vehicle speed must be maintained between a minimum speed limit $v_{\min}$ and a maximum speed limit $v_{\max}$

$$v_{\min}(s) \leq v \leq v_{\max}(s). \quad (6)$$

D. Optimal Control Problem

Let us define a control input vector and a state vector as $u = [u_t, u_b]^T$ and $x = [s, v]^T$, respectively, where $u_t = a_t$ and $u_b = a_b$. To facilitate the derivation of the analytical solution, we made several assumptions. First, assuming a constant road grade ($\alpha(s) = \alpha$) and no transmission loss ($\eta_t = 1$), (1) and (2) are rewritten as

$$\dot{x} = f(x, u, t) = [v, u_t - u_b - c_1 v^2 - c_0]^T \quad (7)$$

where $c_1 = \rho_a A_f c_d/(2m)$ and $c_0 = g(\sin\alpha + c_r \cos\alpha)$.

Then, following [42], Willans' approach is utilized to simplify the engine model, which is used to define a cost function l:

$$l(x, u, t) = \dot{m}_f(v, a_t) \approx p_0 + p_1 a_t v + p_2 v, \quad a_t \geq 0 \quad (8)$$

where the coefficients, p's, are obtained by using the least-square fitting method and given in Table I. Note that a fuel cutoff operation ($a_t = 0$) and ($a_t = 0$), called the pulse-and-glide strategy in [38], avoids the rapid switching between engine ON and OFF states without the cruising mode, which may affect driving comfort.

Finally, the assumption of constant speed limits ($v_{\max}(s) = v_{\max}$ and $v_{\min}(s) = v_{\min}$) allows us to define the following two pure state variable inequality constraints (SVICs):

$$h_1(x, t) = v - v_{\max}(s) \leq 0 \quad (9)$$
$$h_2(x, t) = -v + v_{\min}(s) \leq 0. \quad (10)$$

An OCP that minimizes total fuel consumption is formulated, going from an initial speed, v_0, to a final speed, v_f, over a specified time of t_f and distance of s_f as follows:

$$\min_{u_t, u_b} \quad J = \int_0^{t_f} l(x, u, t) dt$$
$$\text{s.t.} \quad \dot{x} = f(x, u, t)$$
$$h_1(x, t) \leq 0, \quad h_2(x, t) \leq 0 \quad (11)$$

and the BCs are

$$x(0) = x_0 = [s_0, v_0]^T, \quad x(t_f) = x_f = [s_f, v_f]^T. \quad (12)$$

With the given BCs, the total cost over the entire trip can be rewritten by replacing u_t from (7), as shown in the following:

$$J = (p_1 c_0 + p_2)s_f + \frac{p_1(v_f^2 - v_0^2)}{2} + p_0 t_f + p_1 \int_0^{t_f} (c_1 v^3 + u_b v) dt \quad (13)$$

where only the last term is influenced by the control inputs, meaning that such a solution aims at minimizing energy losses

caused by aerodynamic drag and braking. Therefore, we solve the following problem:

$$\min_{u_t, u_b} \int_0^{t_f} (c_1 v^3 + u_b v) dt \quad (14)$$

which is equivalent to the OCP of minimizing "wheel-to-distance" energy losses[1] in [23].

III. BOUNDARY VALUE PROBLEM

A. Inactive SVICs

Following the direct adjoining method (see Appendix A), $\eta = 0$, thus Lagrangian, L, and Hamiltonian, H, are defined as

$$L = H = c_1 v^3 + u_b v + \lambda_1 v + \lambda_2(u_t - u_b - c_1 v^2 - c_0) \quad (15)$$

where λ_1 and λ_2 are the position and speed costates, respectively. Their dynamics are

$$\dot{\lambda}_1(t) = 0 \quad (16)$$
$$\dot{\lambda}_2(t) = -3c_1 v^2 - u_b^* - \lambda_1 + 2 c_1 v \lambda_2. \quad (17)$$

Control inputs are bounded as $0 \leq u_t \leq \bar{u}_t$ and $0 \leq u_b \leq \bar{u}_b$. Let us define $\sigma_1 = \lambda_2$ and $\sigma_2 = v - \lambda_2$. Depending on the sign of the coefficient of linear control terms in the above Hamiltonian, optimal traction and braking control policies (u_t^* and u_b^*) require switching between upper and lower bounds

$$u_t^*(t) = \begin{cases} \bar{u}_t, & \sigma_1 < 0 \\ u_t^s, & \sigma_1 = 0 \\ 0, & \sigma_1 > 0, \end{cases} \quad u_b^*(t) = \begin{cases} \bar{u}_b, & \sigma_2 < 0 \\ u_b^s, & \sigma_2 = 0 \\ 0, & \sigma_2 > 0 \end{cases} \quad (18)$$

where u_t^s and u_b^s denote traction and braking in a possible singular interval, respectively. Using (7) and (17), the switching dynamics ($\dot{\sigma}_1$ and $\dot{\sigma}_2$) can be obtained as

$$\dot{\sigma}_1 = 2c_1 v \sigma_1 - \lambda_{1.0} - 3c_1 v^2 - u_b^* \quad (19)$$
$$\dot{\sigma}_2 = 2c_1 v \sigma_2 + \lambda_{1.0} - c_0 + u_t^* \quad (20)$$

where $\lambda_1(t) = \lambda_1(0) = \lambda_{1.0}$ because of (16). From existence conditions of the singular intervals, $\sigma_i = 0$ and $\dot{\sigma}_i = 0$ for $i = 1, 2$, singular traction control maintains the following constant speed:

$$v_s = \left(-\frac{\lambda_{1.0}}{3c_1}\right)^{\frac{1}{2}} \quad (21)$$

where $u_t^s = c_1 v_s^2 + c_0$. However, singular braking (SB) control cannot be determined in terms of state and costate variables. If the SB interval exists ($\lambda_{1.0} = c_0$), σ_2 must be zero at all times because of the nonnegative eigenvalue of its dynamics ($\dot{\sigma}_2 = 2c_1 v \sigma_2$).

In summary, a combined optimal control policy, $u^* = u_t^* - u_b^*$, is

$$u^*(t) = \begin{cases} \bar{u}_t, & \sigma_1 < 0 \quad \text{(Maximum Acceleration)} \\ u_t^s, & \sigma_1 = 0 \quad \text{(Cruising)} \\ 0, & 0 < \sigma_1 < v \quad \text{(Gliding)} \\ -u_b^s, & \sigma_1 = v \quad \text{(Singular Braking)} \\ -\bar{u}_b, & \sigma_1 > v \quad \text{(Maximum Braking)} \end{cases} \quad (22)$$

[1]The simplified engine model in (8) does not allow for the consideration of complex engine operation efficiency dependencies.

and we formulate the following BVP with BC in (12):

$$\begin{cases} \dot{s} = v \\ \dot{v} = u^* - c_1 v^2 - c_0 \\ \dot{\sigma}_1 = 2\,c_1 v \sigma_1 - \lambda_{1,0} - 3c_1 v^2 + I_A(\sigma_1) u^* \end{cases} \quad (23)$$

where I is the indicator function of a subset $A = \{\sigma_1 \geq v\}$ for the maximum braking and σ_1 is free at both ends.

B. Active SVICs

When SVICs are active, L is defined as (see Appendix A)

$$L = H + \eta_1 h_1 + \eta_2 h_2 \quad (24)$$

where $\eta_i h_i = 0$, $\eta_i \geq 0$ for $i = 1, 2$. Note that H is defined as in (15). Let us consider the h_1 case (the same procedure is applied to the other case). The resulting jump conditions are

$$\begin{cases} \lambda_1(t_j^-) = \lambda_1(t_j^+) \\ \lambda_2(t_j^-) = \lambda_2(t_j^+) + \pi_j \\ H(t_j^-) = H(t_j^+) \end{cases} \quad (25)$$

for $j = 1, 2$, where t_1 and t_2 indicate entry and exit times for the boundary interval control, respectively. We substitute the right-hand side of the above first and second equations for $\lambda_1(t_j^-)$ and $\lambda_2(t_j^-)$ in the above last equation and use the fact of continuous speed at t_j to obtain

$$\sigma_1(t_j^+) \Delta u_t^*(t_j) + \sigma_2(t_j^+) \Delta u_b^*(t_j) + \pi_j \dot{v}(t_j^-) = 0 \quad (26)$$

where $\Delta u_i^*(t_j) = u_i^*(t_j^-) - u_i^*(t_j^+)$, $i = \text{t, b}$. When h_1 is active, the condition, $\sigma_1(t) = 0$ for $t \in [t_1, t_2]$, must be satisfied to generate the cruising mode and then enforce $h_1 = 0$. As the maximum acceleration mode only activates h_1, $u_b^* = 0$ at t_j, which results in $\Delta u_b^*(t_j) = 0$, and $\dot{v}(t_j^-) = \bar{u}_t - c_1 v_{max}^2 - c_0 \neq 0$ at the end. Finally, we got

$$\pi_j = 0 \quad (27)$$

which results in continuous speed and position costates when either h_1 or h_2 is active.

Fig. 1 shows how trajectories are differently generated according to whether h_1 is included in the OCP or not. Without h_1, the vehicle accelerates as much as possible, enters the gliding interval if $\sigma_1 > 0$, and applies the maximum braking if $\sigma_2 < 0$, as shown in (22). On the other hand, with h_1, the cruising mode must be generated to hold $h_1 = 0$ as a result of $\sigma_1 = 0$, while switching states are continuous without any jumps, as shown in (27). Here, the MATLAB BVP solver (collocation method used in [43]) is used to compute fuel-optimal trajectories, but this solver is sensitive to an initial guess and may increase computing times when the SVIC is active. In the following, we present a fast analytical BVP solver that does not require a good initial guess.

IV. ANALYTICAL FUEL-OPTIMAL SOLUTION

A. Feasible Control Sequences

We analyzed the costate dynamics to identify feasible control sequences. As shown in (22), the fuel-optimal control policy determines a control sequence, including five possible intervals such as maximum acceleration (P), cruising (C), gliding (G), SB, and maximum deceleration (B). Analytical
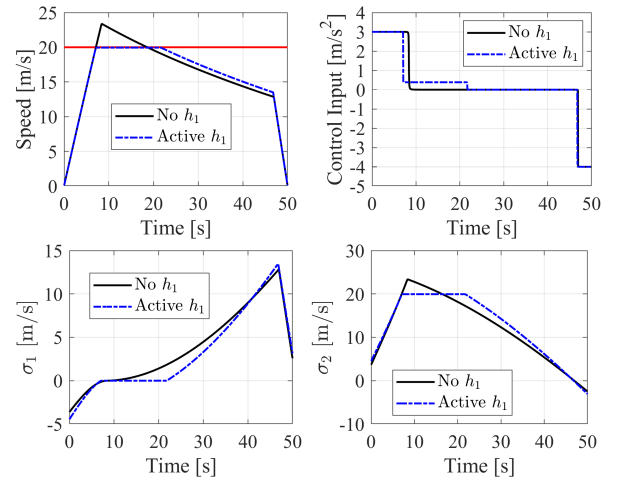

Fig. 1. Fuel-optimal speed (top left) and control input (top right) trajectory corresponding to switching states, σ_1 (bottom left) and σ_2 (bottom right), where $x_0 = [0, 0]^T$, $x_f = [800, 0]^T$, $t_f = 50$, $\bar{u}_t = 3$, $\bar{u}_b = 4$, and $v_{max} = 20$ (red line). Coefficients are the same as in Table I.

TABLE II
FEASIBLE CONTROL SEQUENCES OF EACH SOLUTION

One-interval	Two-interval	Three-interval	Four-interval
P, C, G, B, SB	P-C, P-G, C-P, C-G, G-P, G-C, G-B, B-G	P-C-G, P-C-P, G-C-P, G-C-G, P-G-B, B-G-P	P-C-G-B, G-C-G-B

fuel-optimal solutions can be made up of 1–4 intervals based on the fuel-optimal control policy that considers the switching dynamics (summarized in Table II).

1) One-Interval Solutions: The control sequence includes single interval

$$u^*(t) = u_1. \quad (28)$$

The P, C, G, B, and SB[2] solutions are feasible, where u_1 is set to $\bar{u}_t$, u_t^s, 0, $-\bar{u}_b$, and $-u_b^s$.

2) Two-Interval Solutions: The control sequence consists of two intervals as follows:

$$u^*(t) = \begin{cases} u_3, & [0, t_1) \\ u_4, & [t_1, t_f]. \end{cases} \quad (29)$$

The P-C, P-G, C-P, C-G, G-P, G-C, G-B, and B-G solutions are feasible, where a pair (u_3, u_4) can be set to $(\bar{u}_t, u_t^s)$, $(\bar{u}_t, 0)$, $(u_t^s, \bar{u}_t)$, $(u_t^s, 0)$, $(0, \bar{u}_t)$, $(0, u_t^s)$, $(0, -\bar{u}_b)$, and $(-\bar{u}_b, 0)$, respectively.

3) Three-Interval Solutions: There exist two types of control sequences depending on whether the C interval exists or not as follows:

$$u^*(t) = \begin{cases} u_5, & [0, t_1) \\ u_t^s, & [t_1, t_2) \\ u_6, & [t_2, t_f], \end{cases} \qquad u^*(t) = \begin{cases} u_7, & [0, t_1) \\ 0, & [t_1, t_2) \\ u_8, & [t_2, t_f]. \end{cases} \quad (30)$$

[2]For a one-interval solution where $\sigma_2(t) = 0$ for $t \in [0, t_f]$, the existence conditions of the SB interval can be met. However, for multi-interval solutions, the conditions cannot be met. In such cases, the SB interval needs to be switched from either the B interval or the G interval, where $u_t^* = 0$ for both cases. If the SB interval is switched from the B interval, $\sigma_{2,0} < 0 \rightarrow \dot{\sigma}_2 = 2c_1 v \sigma_2 < 0$. Conversely, if it is switched from the G interval, $\sigma_{2,0} > 0 \rightarrow \dot{\sigma}_2 = 2c_1 v \sigma_2 > 0$. In either case, σ_2 cannot reach zero.

In the former case, the conditions of $\sigma_1 = 0$ and $\dot{\sigma}_1 = 0$ on the C interval allow to switch either the P or G interval depending on terminal conditions, irrespective of the preceding interval. The P-C-G, P-C-P, G-C-P, and G-C-G solutions are feasible, where a pair (u_5, u_6) can be set to $(\overline{u}_t, 0)$, $(\overline{u}_t, \overline{u}_t)$, $(0, \overline{u}_t)$, and $(0, 0)$, respectively. In the latter case, on the other hand, the P-G-B and B-G-P solutions are feasible, where a pair (u_7, u_8) can be set to $-\overline{u}_b$ and $(-\overline{u}_b, \overline{u}_t)$, respectively. Note that the P-G-P, P-G-C, B-G-B, and B-G-C solutions are infeasible (see Appendix B).

4) Four-Interval Solutions: The three-interval solutions including the C interval and ending with the G interval (i.e., P-C-G and G-C-G) may add the B interval to become the four-interval solutions; however, the three-interval solutions ending with the P interval (i.e., P-C-P and G-C-P) cannot generate other intervals (see Appendix C). Therefore, P-C-G-B and G-C-G-B solutions are feasible, and the corresponding control sequence is expressed as

$$u^*(t) = \begin{cases} u_9, & [0, t_1) \\ u_t^s, & [t_1, t_2) \\ u_{10}, & [t_2, t_3) \\ -\overline{u}_b, & [t_3, t_f] \end{cases} \tag{31}$$

where a pair (u_9, u_{10}) can be set to $(\overline{u}_t, 0)$ and $(0, 0)$, respectively.

B. Solution to a System of Nonlinear Equation

Let us denote the ith switching time between ith and $(i+1)$th interval as t_i, $i = 1, \ldots, N-1$, such that $0 = t_0 \leq t_1 \leq \cdots \leq t_{N-1} \leq t_N = t_f$, where N is the number of intervals. On the ith interval $[t_{i-1}, t_i]$, we define time spent as $\xi_i = t_i - t_{i-1}$, where $\sum_{i=1}^{N} \xi_i = t_f$, and ith switching states as the states at t_i, $s_i = s(t_i)$, $v_i = v(t_i)$, and $\sigma_{1.i} = \sigma_1(t_i)$. The fuel-optimal control policy is piecewise constant, and a solution to first-order ODEs in (23) is explicitly derived for each interval (Appendix D); we can determine the ith switching states by substituting variables ξ_i, v_{i-1}, n_i, and $\sigma_{1.i-1}$ for t, v_0, n, and $\sigma_{1.0}$, respectively, in the explicit solutions of $S(t|v_0, n)$, $V(t|v_0, n)$, and $O(t|\sigma_{1.0}, v_0, n)$ as follows:

$$\begin{aligned} s_i &= s_{i-1} + S(\xi_i|v_{i-1}, n_i) \\ v_i &= V(\xi_i|v_{i-1}, n_i) \\ \sigma_{1.i} &= O(\xi_i|\sigma_{1.i-1}, v_{i-1}, n_i) \end{aligned} \tag{32}$$

where n_i is the interval name, $n_i \in \{P, G, B\}$. Note that if $n_i = C$

$$\begin{aligned} S(\xi_i|v_{i-1}, n_i) &= v_{i-1}\xi_i \\ V(\xi_i|v_{i-1}, n_i) &= v_{i-1} \\ O(\xi_i|\sigma_{1.i-1}, v_{i-1}, n_i) &= 0 \end{aligned} \tag{33}$$

where $\sigma_{1.i-1} = 0$. If a control sequence is specified, we can concatenate the ith-interval solution from $i = 1$ to $i = N$ and find N interval times, $(\xi_1, \xi_2, \ldots, \xi_N)$, that satisfy terminal and switching conditions. However, the resulting equations are too complex to solve in a straightforward way.

We convert the complex problem of finding N interval times into the tractable one of finding $(N-1)$ switching speeds

$(v_1, v_2, \ldots, v_{N-1})$. Using V in (32), we obtain its inverse function[3]

$$\xi_i = V^{-1}(v_i|v_{i-1}, n_i) \tag{34}$$

for $n_i \in \{P, G, B\}$. Then, by substituting V^{-1} for ξ_i, we can obtain S and O as a function of the switching speeds, not interval times in (32), and the ith switching states are rewritten as follows:

$$\begin{aligned} s_i &= s_{i-1} + S(v_i|v_{i-1}, n_i) \\ \sigma_{1.i} &= O(v_i|\sigma_{1.i-1}, v_{i-1}, n_i). \end{aligned} \tag{35}$$

The above formulas are given in detail in Appendix E. Note that if $n_i = C$ and $v_i = v_{i-1}$, then

$$\begin{aligned} \xi_i(v_i|v_{i-1}, n_i) &= \xi_i \\ S(v_i|v_{i-1}, n_i) &= v_{i-1}\xi_i \\ O(v_i|\sigma_{1.i-1}, v_{i-1}, n_i) &= 0 \end{aligned} \tag{36}$$

where $\sigma_{1.i-1} = 0$, while an unknown variable is ξ_i, not v_i. Using the above explicit solutions, we can express the terminal conditions as a system of nonlinear equations in $(N-1)$ unknown switching speeds, not switching times

$$\begin{aligned} \sum_{i=1}^{N} \xi_i(v_i|v_{i-1}, n_i) - t_f &= 0 \\ \sum_{i=1}^{N} S(v_i|v_{i-1}, n_i) - s_f &= 0. \end{aligned} \tag{37}$$

Note that coefficients k in this section and the following section are defined in Appendix D.

For three-interval solutions $(N = 3)$, two unknown switching speeds are directly found by solving (37). Given the specified control sequence, finding switching speeds is decoupled from finding initial costates. We find switching speeds, compute the corresponding switching times, and use them to find initial costates that satisfy switching conditions in a sequential manner. For example, the P-G-B solution provides the following system of two nonlinear equations:

$$\begin{aligned} \xi_1(v_1|v_0, P) + \xi_2(v_2|v_1, G) + \xi_3(v_f|v_2, B) - t_f &= 0 \\ S(v_1|v_0, P) + S(v_2|v_1, G) + S(v_f|v_2, B) - s_f &= 0. \end{aligned} \tag{38}$$

Using the solution to this system, v_1 and v_2, we express the corresponding switching conditions as $\sigma_{1.1} = O_1(v_1|\sigma_{1.0}, v_0, P) = 0$ and $\sigma_{1.2} = O_2(v_2|\sigma_{1.1}, v_1, G) = v_2$. By solving these equations, initial costates are expressed as

$$\begin{aligned} \lambda_{1.0} &= -k_1^2(k_4^2 v_1 + v_0^3)/(v_0 - v_1) \\ \sigma_{1.0} &= (k_4^2 v_1 + v_1^3)/(k_2^2 - v_0^2). \end{aligned} \tag{39}$$

For four-interval solutions $(N = 4)$, an active condition of the B interval at the end of C-G sequence, is required to find three switching speeds in addition to (37):

---

[3]The function V in the P interval is monotonic. In the G and B intervals, the function V is monotonic only if $t \in [(k_5 - \pi/2)/(k_1^2 k_4), (k_5 + \pi/2)/(k_1^2 k_4)]$, but the feasible t range is $[0, k_5/(k_1^2 k_4)]$ when considering nonnegative speeds. As a result, both functions are considered as one-to-one functions.

$O(v_i|\sigma_{1.i-1}, v_{i-1}, G) - v_i = 0$. By using (72), this condition is rewritten as

$$2v_{i-1}^3 - 3v_i v_{i-1}^2 - k_4^2 v_i = 0. \tag{40}$$

For example, the P-C-G-B solution provides the following system of three nonlinear equations in two unknown switching speeds (v_1, v_3) and one unknown length of the C interval (ξ_2):

$$\xi_1(v_1|v_0, P) + \xi_2 + \xi_3(v_3|v_2, G) + \xi_4(v_f|v_3, B) - t_f = 0$$
$$S(v_1|v_0, P) + v_1\xi_2 + S(v_3|v_2, G) + S(v_f|v_3, B) - s_f = 0$$
$$2v_2^3 - 3v_3v_2^2 - k_4^2v_3 = 0 \tag{41}$$

where $v_2 = v_1$. Using v_1 as one of the solutions to this system, we express the corresponding switching conditions as $\sigma_{1.1} = O(v_1|\sigma_{1.0}, v_0, P) = 0$. By solving this equation, initial costates are expressed as

$$\lambda_{1.0} = -3k_1^2v_1^2$$
$$\sigma_{1.0} = -(v_0^3 - 3v_0v_1^2 + 2v_1^3)/(k_2^2 - v_0^2). \tag{42}$$

Note that once the system of nonlinear equations is obtained, these equations can be simplified to one equation for one variable by substituting the other variables one by one, and thus, the resulting equation can be easily solved.

C. Relationship With BCs

BCs consist of v_0, s_f, v_f, and t_f, given $s_0 = 0$ and $t_0 = 0$, and they determine a control sequence. Fig. 2 shows seven types of solution transition determined by (t_f, v_f), where for each type, a solution changes its control sequence as s_f changes. First, we present five conditions using (t_f, v_f) to classify the solution transition type into seven groups. Then, we establish a feasible region of (t_f, v_f) for each type and show a transition-type selection process. Finally, a solution selection process is addressed by introducing a feasible range of s_f for each solution.

1) Five Conditions: Condition 1 is set by whether the B interval is required to satisfy $v(t_f) = v_f$ or not. Using the G solution, we obtain its minimum final time such that v_f can be reached through only G interval

$$t_f \geq t_{f.th.1}(v_f) = \xi_1(v_f|v_0, G)$$
$$\rightarrow f_{th.1}(t_f, v_f) = t_f - t_{f.th.1}(v_f) \geq 0. \tag{43}$$

If $f_{th.1} < 0$, the B interval must be included in the control sequence, and notably, the SB solution can be generated.

Condition 2 is set by whether the P interval is required to satisfy $v(t_f) = v_f$ or not, which simply gives

$$v_f \geq v_{f.th.2} = v_0. \tag{44}$$

If $v_f \geq v_{f.th.2}$, the P interval must be included, i.e., both G-C-G and G-C-G-B solutions cannot be generated; otherwise, the P-C-P solution cannot be generated.

Condition 3 and 4 are set by whether the B interval is active at the end of the last G interval for the G-C-G and P-C-G solutions when increasing s_f. These two solutions may additionally activate the B interval when $\sigma_1 \geq v$ as a result of the increase in s_f. Let us assume that these two solutions
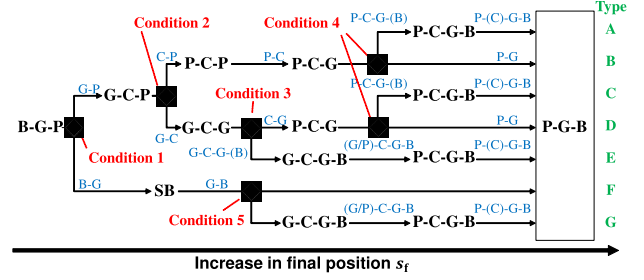

Fig. 2. Schematic for seven types of transition between control sequences of analytical solutions as s_f changes (1–7 from top to bottom, highlighted in green).

do not have the B interval even if s_f increases. The G-C-G solution diminishes the first G interval length (i.e., $\xi_1 \rightarrow 0$ and $v_2 = v_1 \rightarrow v_0$) and becomes the C-G solution, followed by the P-C-G solution. On the other hand, the P-C-G solution diminishes the C interval length (i.e., $\xi_2 \rightarrow 0$) and becomes the P-G one, followed by the P-G-B solution. Both C-G and P-G solutions must satisfy the condition of $\sigma_{1.3} < v_f$, to hold the assumption. If not, the B interval must be made. From this point, the condition to activate the B interval is derived from $\sigma_{1.3} = O(v_3|0, v_2, G) \geq v_f$ and (72) as follows:

$$g(v_2) = 2v_2^3 - 3v_fv_2^2 - k_4^2v_f \geq 0. \tag{45}$$

As the C-G solution provides $v_2 = v_1 = v_0$, $g(v_0) \geq 0$. We can set Condition 3 for v_f to exist the G-C-G-B solution

$$v_f \leq v_{f.th.3} = 2v_0^3/(k_4^2 + 3v_0^2) \tag{46}$$

where $v_{f.th.3} < v_{f.th.2}$. The P-G solution provides $v_2 = v_1$, but v_2 is dependent on v_f and t_f. From the cubic function $g(v_2) = 0$, where it always has one real root (v_r) and two nonreal complex conjugate roots, we consider v_r as a minimum v_2, i.e., $v_2 \geq v_r$, to ensure $g(v_2) \geq 0$. Given $v_2 = v_r$, we can compute the corresponding minimum t_f and set Condition 4 for t_f to exist the P-C-G-B solution because v_2 increases with t_f for the given v_f as follows:

$$t_f \geq t_{f.th.4}(v_f) = \xi_1(v_r|v_0, P) + \xi_3(v_f|v_r, G)$$
$$\rightarrow f_{th.4}(t_f, v_f) = t_f - t_{f.th.4}(v_f) \geq 0 \tag{47}$$

where $\xi_2 = 0$.

Note that Condition 3 guarantees that the P-C-G-B solution exists as well. Using (46), $g(v_2) \geq 0$ can be proved as follows:

$$g(v_2) \geq \frac{6v_2^2v_0^2(v_2 - v_0) + 2k_4^2(v_2^3 - v_0^3)}{k_4^2 + 3v_0^2} \geq 0 \tag{48}$$

where $v_2 = v_1 \geq v_0$.

Condition 5 is set by whether the G-C-G-B solution exists next to the SB solution when increasing s_f. As s_f decreases, the P-G-B solution diminishes the P interval length (i.e., $\xi_1 \rightarrow 0$ and $v_1 \rightarrow v_0$), whereas the G-C-G-B solution diminishes the C interval length (i.e., $\xi_2 \rightarrow 0$); they become the G-B solution. The G-B solution from the G-C-G-B solution must hold the condition of $v_2 = v_1 \leq v_0$ as other G-B solution ends up with $v_1 = v_0$. Given $v_2 = v_1 = v_0$, we can compute the
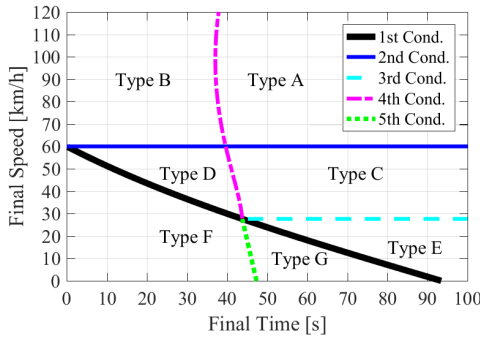
Fig. 3. Seven transition types in the plot of final time (t_f) and final speed (v_f) classified by five conditions in case of $v_0 = 60$ km/h.

corresponding minimum t_f, which gives the fifth condition for t_f to exist the G-C-G-B solution

$$t_f \geq t_{f.th.5}(v_f) = \xi_3(v_3|v_0, G) + \xi_4(v_f|v_3, B)$$
$$\rightarrow f_{th.5}(t_f, v_f) = t_f - t_{f.th.5}(v_f) \geq 0 \qquad (49)$$

where $v_3 = 2v_2^3/(k_4^2 + 3v_2^2)$, derived by (40), and $\xi_1 = \xi_2 = 0$.

2) Transition-Type Selection: In summary, using five conditions, we establish a feasible region of (t_f, v_f) for each transition type

$$\text{Type}(t_f, v_f)$$

$$= \begin{cases} A, & f_{th.1} \geq 0, \ f_{th.4} \geq 0 & v_f \in [v_{f.th.2}, \infty] \\ B, & f_{th.1} \geq 0, \ f_{th.4} < 0 & v_f \in [v_{f.th.2}, \infty] \\ C, & f_{th.1} \geq 0, \ f_{th.4} \geq 0 & v_f \in [v_{f.th.3}, v_{f.th.2}] \\ D, & f_{th.1} \geq 0, \ f_{th.4} < 0 & v_f \in [v_{f.th.3}, v_{f.th.2}] \\ E & f_{th.1} \geq 0 & v_f \in [0, v_{f.th.3}] \\ F, & f_{th.1} < 0, \ f_{th.5} < 0 & \\ G, & f_{th.1} < 0, \ f_{th.5} \geq 0. & \end{cases} \qquad (50)$$

Fig. 3 shows seven transition types classified by five conditions in the plot of final time versus final speed, given $v_0 = 60$ km/h. All types are categorized into three groups by Condition 1 (black bold line) and Condition 2 (blue line): Group 1 (Types A and B), Group 2 (Types C, D, and E), and Group 3 (Types F and G). Group 1 requires the P interval, whereas Group 3 requires the B interval. Then, the remaining three conditions (cyan dashed line, magenta dashed-dotted line, and green dotted line) can distinguish between all types included in Groups 1–3. For example, we can select Type C among seven transition types when $(t_f, v_f) = (60 \text{ s}, 40 \text{ km/h})$.

3) Solution Selection: After one transition type is selected by (t_f, v_f), the remaining s_f determines the solution. To this end, we establish a feasible s_f range of each solution by computing its minimum and maximum travel distance. As shown in Fig. 2, each solution generally vanishes one interval by diminishing its length to maximize or minimize its travel distance, e.g., the B-G-P solution becomes the G-P one for maximum s_f in Type A (i.e., $\xi_1 \rightarrow 0$ and $v_1 \rightarrow v_0$). Note that solutions of these extreme cases are highlighted in blue color, where the interval in bracket for the four-interval solutions indicates vanished one. These extreme cases where one of the intervals, denoted by the pth interval, is vanished, add the
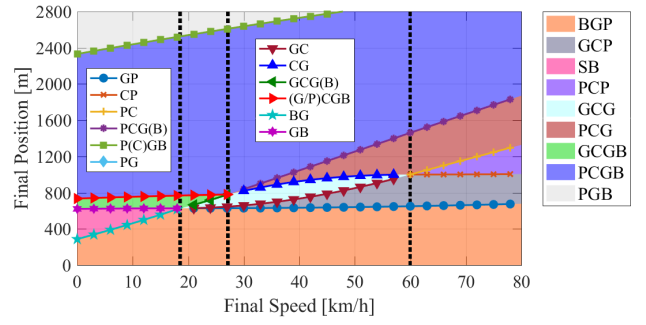

Fig. 4. Feasible s_f range of each solution depending on the final speed in the case of $v_0 = 60$ km/h and $t_f = 60$ s.
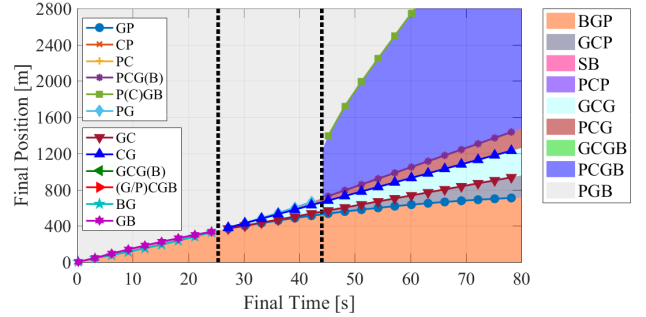

Fig. 5. Feasible s_f range of each solution depending on the final time in the case of $v_0 = 60$ km/h and $v_f = 40$ km/h.

following condition:

$$\xi_p = 0 \quad \text{for } n_p = C$$
$$\begin{cases} v_1 = v_0 & p = 1 \\ v_{N-1} = v_f & p = N \end{cases} \quad \text{for } n_p \in \{B, G, P\}. \qquad (51)$$

Thus, we can use the above condition instead of using the second condition in (37) to find switching speeds and times of three- and four-interval solutions. Then, using these switching speeds and times, we compute the resulting travel distance (D) and define it as the minimum and maximum s_f as follows:

$$D(n_1^*, \ldots, n_{N-1}^*) = \sum_{i=1}^{N} S(v_i|v_{i-1}, n_i) \qquad (52)$$

where $S(v_p|v_{p-1}, n_p) = 0$ and n_i^* indicates the remaining interval, defined by $n_i^* = n_i$ if $i < p$ and $n_i^* = n_{i-1}$ if $i > p$. For $N = 3$, $(n_1^*, n_2^*) = (G, P)$, (B, G), (C, P), (G, C), (P, C), (C, G), (G, B), (P, G), while for $N = 4$, $(n_1^*, n_2^*, n_3^*) = (G, C, G)$, (P, C, G), (C, G, B), (P, G, B).

Given $v_0 = 60$ km/h, Figs. 4 and 5 show a feasible s_f range of each solution depending on v_f (given $t_f = 60$ s) and t_f (given $v_f = 40$ km/h), respectively, where this range is defined as the area in the planes, (v_f, s_f) and (t_f, s_f), between the minimum and maximum curves. In Fig. 4, Conditions 1–3 with $t_f = 60$ s provide $v_{f.th.1} = 18.5$ km/h, $v_{f.th.2} = 60$ km/h, and $v_{f.th.3} = 27.1$ km/h, respectively (see Fig. 3); this implies four possible transition types depending on v_f: Type G ($[0, v_{f.th.1}]$), Type E ($[v_{f.th.1}, v_{f.th.3}]$), Type C ($[v_{f.th.3}, v_{f.th.2}]$), and Type A ($[v_{f.th.2}, \infty]$). On the other hand, in Fig. 5, Conditions 1 and 4 with $v_f = 40$ km/h provide $t_{f.th.1} = 25.4$ s and $t_{f.th.4} = 44.1$ s, respectively, which gives three transition types depending on t_f: Type F ($[0, t_{f.th.1}]$), Type D ($[t_{f.th.1}, t_{f.th.4}]$), and Type C ($[t_{f.th.4}, \infty]$).
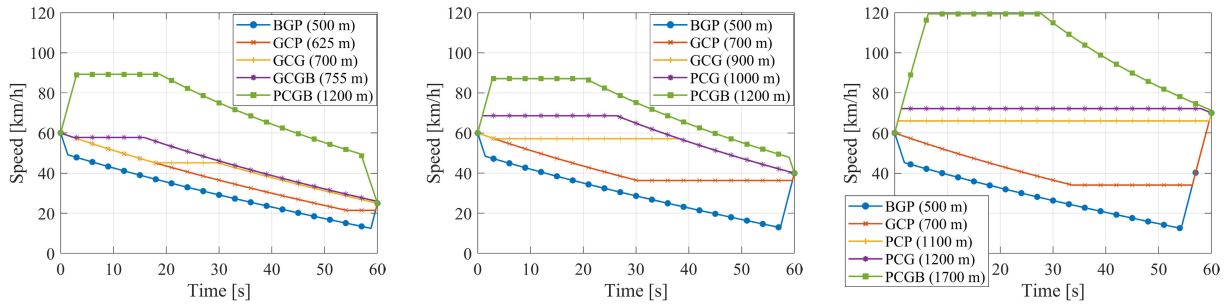
Fig. 6. Fuel-optimal speed profiles when increasing s_f for three final speed conditions: $v_f = 25$ km/h (left), $v_f = 40$ km/h (middle), and $v_f = 70$ km/h (right), given $t_f = 60$ s.

Fig. 6 shows how the control sequence changes when increasing s_f while satisfying the desired final speed and final time. In addition, three final speed conditions give rise to distinct types of transition (Types A, C, and E), each of which induces specific changes in the control sequence. Adhering to the optimal control policy results in these changes, as the policy relies on the switching state variables computed by their dynamics with initial values that are intended to satisfy the terminal state conditions. For example, the given three-tuple $(t_f, v_f, v_0) = (60$ s, 40 km/h, 60 km/h) selects Type C (see Fig. 3) where the control sequence changes in the following order as s_f increases: B-G-P, G-C-P, G-C-G, P-C-G, P-C-G-B, and P-G-B. The condition of $s_f = 900$ m is in the feasible s_f range of the G-C-G solution (the light blue shaded area in Figs. 4 and 5) established by its minimum and maximum s_f curves computed by the G-C and C-G solutions, respectively. Thus, the G-C-G control sequence is selected to compute the fuel-optimal solution.

D. Speed Limit Constrained Solution

If the selected solution may violate the maximum/minimum speed limit constraint, we must use a speed limit constrained solution that has a boundary interval, i.e., C interval, to keep the maximum/minimum speed limit. Theoretically, η_1 and η_2 introduced in (24) are included in the $\lambda_2 (=\sigma_1)$ dynamics by the optimality conditions in (60). When maximum/minimum speed limit constraint is active, η_1 or η_2 jumps to some value from zero such that $\dot{\sigma}_1 = 0$, thereby generating the C interval at the maximum/minimum speed limit. When one of the P-G-B, P-C-G-B, and P-C-G solutions generates the speed greater than the maximum speed limit, it must be changed to the P-C-G-B solution, including the C interval at the maximum speed limit. On the other hand, when one of the B-G-P and G-C-P solutions generates the speed lower than the minimum speed limit, it must be changed to the B-G-C-P solution, including the C interval at the minimum speed limit. Note that the infeasible B-G-C-P solution (see Appendix B) becomes feasible when the minimum speed limit constraint is active because of the η_2 jump. Finally, the speed limit constrained solutions can be computed based on the specified control sequence in the same way as in the unconstrained four-interval solutions.

E. Feasible Terminal Conditions

Final speed and position conditions must be feasible to compute analytical fuel-optimal solutions. This feasibility can be set by control input and speed constraints. Let us assume the extreme case where the one-interval solution has either the B or P interval (i.e., the control input constraint is active over the entire time). The resulting speed at the final time and speed limits is used to set a feasible condition for v_f

$$v_{f.\,min} \le v_f \le v_{f.\,max} \tag{53}$$

where $v_{f.\,min} = \max(V(t_f|v_0, \text{B}), v_{min})$ and $v_{f.\,max} = \min(V(t_f|v_0, \text{P}), v_{max})$.

To set a feasible condition for s_f, we consider two cases: control input constraints are active and both control input and speed constraints are active. The first case uses the two-interval solutions such as the B-P and P-B solutions to obtain the resulting position at the final time, $D(\text{B}, \text{P})$ and $D(\text{P}, \text{B})$ in (52). Note that v_1 can be computed by solving the final time condition in (37). The second case uses the three-interval solutions such as the B-C-P and P-C-B solutions, including the C interval at speed limits to obtain the resulting position at final time, $D(\text{B}, \text{C}, \text{P})$ and $D(\text{P}, \text{C}, \text{B})$ in (52). Note that $v_1 = v_2 = v_{min}$ and $v_1 = v_2 = v_{max}$ in the case of B-C-P and P-C-B solutions, respectively, and then, ξ_2 can be computed by solving the final time condition in (37). Thus, the feasible condition for s_f is set by

$$s_{f.\,min} \le s_f \le s_{f.\,max} \tag{54}$$

where $s_{f.\,min} = \max(D(\text{B}, \text{P}), D(\text{B}, \text{C}, \text{P}))$ and $s_{f.\,max} = \min(D(\text{P}, \text{B}), D(\text{P}, \text{C}, \text{B}))$.

F. Discussion

We evaluated the accuracy and computing times of the proposed analytical solver (see the pseudocode in Algorithm 1) compared with the nonlinear optimization method. We first discretized and converted the fuel-optimal speed control problem described in Section II to a nonlinear programming (NLP) problem. The resulting NLP problem is formulated and solved by using the "fmincon" function with the sequential quadratic programming algorithm from the MATLAB optimization toolbox. We obtained NLP solutions for different grid sizes. As shown in Fig. 7, there exists a tradeoff between computing time and fuel consumption, meaning that as the number of grid points increases, computing time also increases, but the resulting fuel consumption is reduced. On the other hand, the proposed analytical solver does not require the discretization and uses explicit ODE solutions to compute trajectories; thus, it can guarantee the lowest computing time of less than
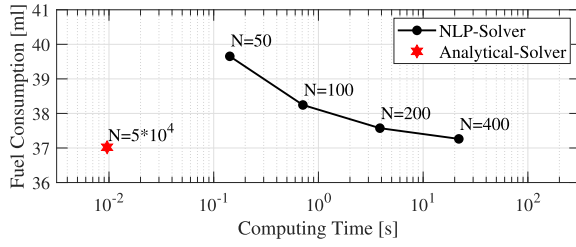
Fig. 7.   Comparison between the proposed analytical solver and MATLAB NLP-based solver with different grid sizes of $N = (50, 100, 200, 400)$. All conditions without the maximum speed limit are the same as in Fig. 1 and fuel consumption is computed by (5).

Algorithm 1 Pseudocode

Input: $s_0, v_0, t_0, s_f, v_f, t_f, v_{\min}, v_{\max}, \overline{u}_t, \overline{u}_b$
Output: $s^*(t), v^*(t), a^*(t)$ for $t \in [t_0, t_f]$

1 $t_f = t_f - t_0$, $s_f = s_f - s_0$
2 compute the terminal state limits ($s_{f.\min}$, $s_{f.\max}$, $v_{f.\min}$ and $v_{f.\max}$) using (53, 54) and update (s_f, v_f)
3 compute all threshold conditions ($f_{th.1}$, $v_{th.2}$, $v_{th.3}$, $f_{th.4}$, $f_{th.5}$) using (43, 44, 46, 47, 49)
4 select one transition type for (t_f, v_f) using (50)
5 compute the feasible s_f range of each solution type included in the selected transition type using (52)
6 select one solution type for s_f
7 find switching speeds by solving the system of nonlinear equations, e.g., (38), (41), and then compute the switching times
8 compute the trajectories using V and S in (67, 68) with each interval end points
9 **if** *speed trajectory violates the limits* **then**
10   select the speed limit-constrained solution type and go back to the step 7.
11 $t_f = t_f + t_0$, $s^*(t) = s_0 + s^*(t)$

---

10 ms irrespective of the grid size and the high accuracy providing the lowest fuel consumption. Note that the NLP solver can bring the additional fuel savings by considering road slope profile in hilly roads, which cannot be achieved by the proposed solver assuming the zero road slope.

V. SIMULATION STUDY AND ANALYSIS

A. Baseline and Fuel-Optimal Speed Controller

As a baseline controller, we used the intelligent driver model (IDM), which is widely accepted as a car-following model for traffic flow studies [44]. The IDM computes acceleration/deceleration, denoted by a_{IDM}, within comfortable acceleration/deceleration limits while preventing collisions with the preceding vehicle in car-following scenarios. The acceleration/deceleration of the next step, a_n, is the same as a_{IDM} computed by the following equation:

$$a_n = a_{IDM} = a_c \left[1 - \left(\frac{v}{v_d} \right)^\delta - \left(\frac{d_{r.d}}{d_r} \right)^2 \right] \quad (55)$$

where

$$d_{r.d} = d_{\min} + \max\left(0, vT + \frac{vv_r}{2\sqrt{a_c b_c}} \right) \quad (56)$$

and d_r and v_r are relative distance and speed to the preceding obstacles/vehicles, respectively ($d_r = s_p - s$, $v_r = v - v_p$, where s_p and v_p are position and speed of the preceding obstacles/vehicles, respectively), and $d_{\min}$, T, a_c, b_c, and v_d are the minimum safe gap, the time gap, the comfortable acceleration and deceleration, and the desired speed, respectively. The parameters are set as $d_{\min} = 2$ m, $T = 1$ s, $a_c = 1.5$ m/s^2, $b_c = 2$ m/s^2, and $\delta = 4$.

On the other hand, a fuel-optimal speed controller uses the proposed fuel-optimal solutions to compute vehicle states trajectories (position, speed, and acceleration/deceleration) at every sampling step ($= 0.1$ s); then, it applies the fuel-optimal acceleration/deceleration of next step, denoted by $a_{n.o}$, in the MPC scheme fashion.[4] To avoid collisions with preceding vehicles in car-following scenarios, we limit $a_{n.o}$ by using a_{IDM} as follows:

$$a_n = \min(a_{n.o}, a_{IDM}) \quad (57)$$

where $a_c = \overline{u}_t$, $b_c = \overline{u}_b$, and $T = 0.5$ s to maximize fuel-saving potentials while guaranteeing safety. Note that any car-following models can be used for limiting $a_{n.o}$.

In this article, vehicles equipped with the baseline controller and vehicles equipped with the fuel-optimal speed controller are called human-driven vehicles (HVs) and CAVs, respectively. Using the original engine model in (5), fuel savings with respect to the HVs are computed by

$$\text{Fuel Savings} = \frac{\sum_{i=1}^{N} m_{f.b}^{(i)} - \sum_{j \in \Omega_b, k \in \Omega_o} \left(m_{f.b}^{(j)} + m_{f.o}^{(k)} \right)}{\sum_{i=1}^{N} m_{f.b}^{(i)}} \quad (58)$$

where $m_{f.b}$ and $m_{f.o}$ are fuel consumed by HVs and CAVs, respectively, N is total number of vehicles in the scenario, and Ω_b and Ω_o are sets of HVs and CAVs, respectively.

We considered the two types of a typical urban driving scenario where vehicles travel a link between two intersections (e.g., stop signs) in the desired travel time (i.e., final time) for comparison between HVs and CAVs: single-vehicle scenarios in free-flow conditions and multiple-vehicle scenarios in car-following situations. Initial and final speeds are set to zero, and the travel distance (i.e., final position) is fixed as 1000 m.

B. Single-Vehicle Scenarios

Single-vehicle scenarios without a preceding vehicle allow us to analyze the maximum fuel savings of CAV. Theoretically, the more aggressive the acceleration/deceleration limits are set, the higher the fuel savings will be. However, these limits should be balanced by considering driving comfort (see Appendix F for further details on the direct consideration of driving comfort in the OCP). Fig. 8 shows fuel savings depending on final time between 55 and 75 s for three different levels of acceleration/deceleration limits (mild: $\overline{u}_t = \overline{u}_b = 2$,

---

[4]Properly determining the final time t_f is important in achieving both eco-driving and human-like driving. One approach to determining t_f is to use the maximum speed limit, with a tunable speed ratio or a real-time average speed obtained from an intelligent navigation system based on the desired distance. Once t_f is determined, its value should be gradually reduced to zero (shrinking horizon control), rather than using a fixed value like receding horizon control.
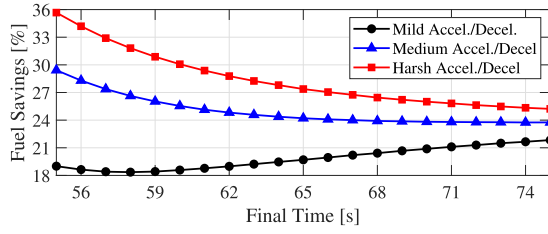
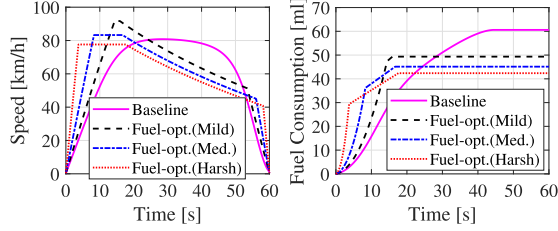Fig. 8. Fuel savings depending on final time as well as acceleration/deceleration level: $s_f = 1000$ m.

Fig. 9. Speed (left) and fuel consumption (right) trajectories depending on acceleration/deceleration level: $t_f = 60$ s and $s_f = 1000$ m.

medium: $\overline{u}_t = \overline{u}_b = 3$, and harsh: $\overline{u}_t = \overline{u}_b = 6$). Note that we searched v_d of IDM so that HVs can arrive at the next stop signs at the same desired travel time. It can be seen that energy savings are higher for high-speed driving induced by the lower final time.

Compared to HVs, CAVs can maximize the engine operation efficiency by full propulsion in a short time at the beginning of the trip and then take advantage of the G interval to finish the trip; thus, it can save fuel by more than 20% on average. As can be seen in Fig. 9, all CAVs with different levels do not use any more fuel since they start coasting, whereas HVs continuously use fuel over time, leading to the highest fuel consumption. The case with the harsh acceleration level can reach the desired speed fastest and brake for a stop the latest, generating the lower cruising speed while keeping a long G interval length. This is the main reason why more aggressive acceleration/deceleration saves fuel more.

Fig. 10 shows how the control sequence and its corresponding interval change with different final time values and acceleration/deceleration levels. Generally, the P interval length and the B interval length decrease as the final time increases. If maximum acceleration/deceleration is sufficiently high (medium and harsh levels), the C and G intervals coexist; otherwise, the C interval cannot be generated with low final time because the solution requires a long P interval to reach high speed. As the final time increases, the G interval length decreases, but the C interval length increases to meet the desired travel distance (mild and medium levels).

These observations can inform an intelligent determination of the final time based on the expected fuel savings for given scenarios. By optimizing the final time in this way, we can achieve significant fuel savings while balancing driving comfort and other constraints such as the desired travel time.

C. Multiple-Vehicle Scenarios With Different PRs

Ten vehicle scenarios allow us to analyze how much fuel CAVs can save, in the presence of the preceding vehicles
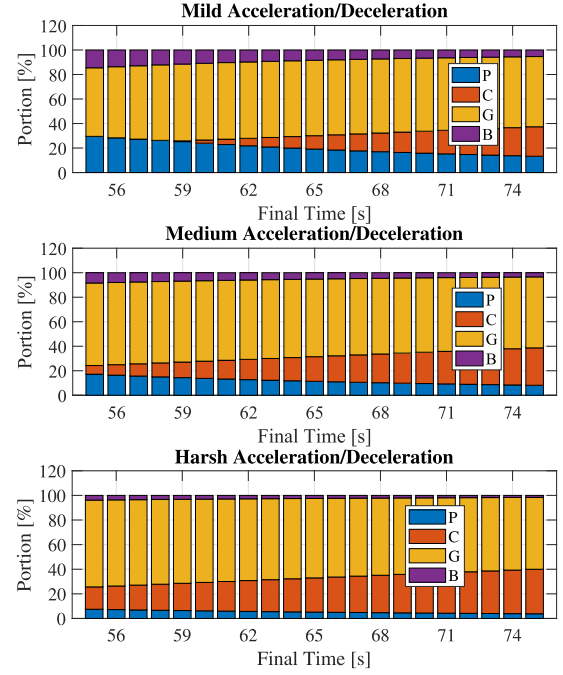

Fig. 10. Portion of P, C, G, and B intervals in fuel-optimal solutions depending on final time: mild level (top), medium level (middle), and harsh level (bottom).
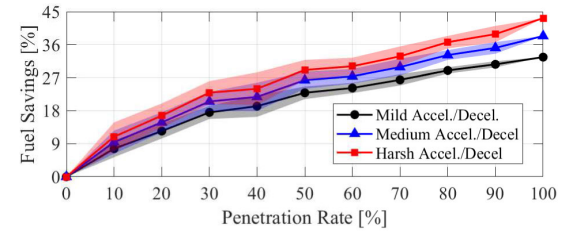

Fig. 11. Fuel savings depending on different PRs of CAVs with three levels of acceleration/deceleration. The lines describe the average fuel savings of ten simulations for the given PR, and the corresponding shaded area indicates the ± standard deviation.

and also how they affect driving behaviors of the following vehicles. To this end, we considered ten different PRs of CAVs from 0% to 100% (i.e., the percentage of CAVs for a total of ten vehicles). For the given PR, ten simulations are performed for high reliability, i.e., ten different sequence orders of vehicles, including CAVs, are randomly generated: e.g., 1-0-0-1-0-0-0-0-0-0 (lead) versus 0-0-0-1-0-0-0-0-1-0 (lead) for the given 20% PR, where 0 and 1 indicate HV and CAV, respectively.

Fig. 11 shows the average fuel savings compared to the case of 0% PR. Note that the desired travel times of CAVs are set to those obtained from 0% PR case where v_d of IDM is fixed as 24 m/s. As expected, the case of 100% PR results in the highest fuel savings, and more aggressive acceleration/deceleration level leads to higher average fuel savings. Fuel savings differ depending on the sequence order of vehicles for the given PR. In particular, fuel savings of more aggressive acceleration/deceleration are spread over a wider range (e.g., the standard deviation of mild, medium, and harsh levels at 40% PR is 2.91%, 3.87%, and 4.46%, respectively).
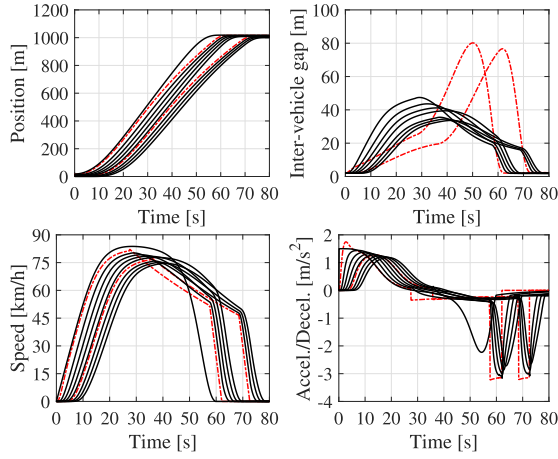
Fig. 12. Position (top left), intervehicle gap (top right), speed (bottom left), and acceleration/deceleration (bottom right) trajectories of ten vehicles in the best case of 20% PR of CAVs with medium level of acceleration/deceleration: two CAVs (dashed-dotted red line) and eight HVs (black line).
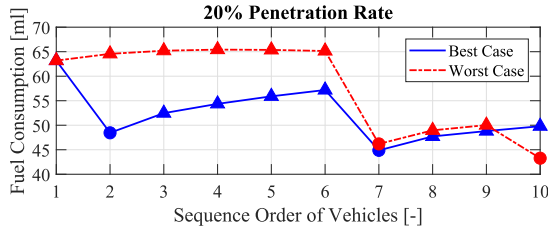

Fig. 13. Fuel consumption of ten vehicles in case of 20% PR of CAVs with medium level of acceleration/deceleration. The best and worst cases indicate the cases resulting in the maximum and minimum value of total fuel consumption for ten simulations, respectively. Triangle and circle points indicate HVs and CAVs, respectively.

Fig. 12 shows the state trajectories of the best case resulting in the highest fuel savings for ten different sequence orders, given 20% PR. All vehicles can finish the trip without collisions with the preceding vehicles. As a result of car following, two CAVs (the second and seventh order) limited their acceleration lower than the maximum value in the beginning. Then, they coast down to a lower speed and increase the intervehicle gap instead of following the preceding vehicle. This coasting leads to the following vehicles to have a coasting behavior as well. In Fig. 13, every point indicates the fuel consumption of each vehicle for the best and worst cases considering 20% PR. Each CAV significantly decreases its fuel consumption compared to the preceding HV; moreover, the HVs behind can mimic the fuel-optimal driving by following the CAV. CAVs act like a speed advisory system that enables the HVs in behind to coast down partially and eventually save fuel further. It is worth noting that as PR increases and CAVs are followed by more HVs (i.e., the leading position of the fleet), CAV's impact on fuel savings of HVs is more magnified.

VI. CONCLUSION

In this article, we proposed a fast analytical solver through the following steps: formulate a fuel-OCP, derive a BVP, and obtain a system of nonlinear equations. Note that this procedure can be applied to develop analytical solvers for any energy-efficient control problem. From the analysis of costate dynamics in BVP, we identified feasible control sequences of

fuel-optimal solutions and established a feasible range of BC for each control sequence including multiple modes. For each mode where the control variable is constant, an explicit ODE solution, including nonlinearity caused by aerodynamic drag resistances, is derived and used to compute the state trajectory without increasing computing complexity. Results show that as an acceleration/deceleration level decreases, CAVs' trajectory becomes more practical while still leading to significant fuel savings. For ten vehicle scenarios, fuel savings of CAVs increase with their PRs and also benefit HVs that follow CAVs. This benefit is maximized as more HVs are driving behind CAVs.

We would like to evaluate the robustness of the proposed analytical solver for various real-world scenarios (e.g., urban corridor scenarios consisting of multiple intersections and lanes) in terms of fuel, traffic flow, vehicle safety, and so on. Then, we would like to implement it in an experimental automated vehicle and validate its effectiveness through various experiment testing.

APPENDIX A
DIRECT ADJOINING METHOD

The direct adjoining method based on PMP can address the OCP with SVIC defined by $h(x, t) \leq 0$ in [45]. When the SVIC is active, there exists a subinterval that satisfies $h(x, t) = 0$ for $t \in [t_1, t_2]$ with $t_1 < t_2$, called a boundary interval (t_1 and t_2 are entry time and exit time, respectively), or a point satisfying $h(x, t_1) = 0$, called a contact point (t_1 is contact time). Note that the entry, exit, and contact times are called junction times. Following the direct adjoining method, the Hamiltonian H is defined first, and then, the SVIC is directly adjoined in H to form the Lagrangian L as follows:

$$H = l + \lambda f, \quad L = H + \eta h \tag{59}$$

where λ is a costate variable and η is a Lagrangian multiplier. The optimality conditions are

$$L_u = 0, \quad \dot{\lambda} = -L_x \tag{60}$$

where $\eta \geq 0$ and $\eta h = 0$. Jump conditions at junction times t_j are

$$\lambda(t_j^-) = \lambda(t_j^+) + \pi_j h_x(x, t_j)$$
$$H(t_j^-) = H(t_j^+) - \pi_j h_t(x, t_j) \tag{61}$$

where π_j is a jump parameter that satisfies the conditions of $\pi_j \geq 0$ and $\pi_j h(x, t_j) = 0$, and t_j^- and t_j^+ are the left-hand side and the right-hand side of t_j, respectively; h_x and h_t are partial derivative of h with respect to the variable x and t, respectively.

APPENDIX B
FEASIBLE P-G-B AND B-G-P SOLUTIONS

To switch the G interval from either the P interval ($i = 1$) or the B interval ($i = 2$), conditions of $\sigma_i(t_1) = 0$ and $\dot{\sigma}_i(t_1) > 0$ must be satisfied. Using (19) and (20), these conditions provide

$$\lambda_{1.0} < -3c_1 v(t_1)^2 \quad \text{for P-G case} \tag{62}$$
$$\lambda_{1.0} > c_0 \quad \text{for B-G case.} \tag{63}$$

By substituting for $\lambda_{1.0}$ by using (19) and (20), the above inequality constraints become

$$
\begin{cases}
\dot{\sigma}_1 > 2c_1 v \sigma_1 + 3c_1\big(v(t_1)^2 - v^2\big) \\
\dot{\sigma}_2 < 2c_1\big(v\sigma_2 - v(t_1)^2\big) - c_1 v(t_1)^2 - c_0, & \text{for P-G case} \\
\dot{\sigma}_1 < 2c_1 v(\sigma_1 - v) - c_0 - c_1 v^2 \\
\dot{\sigma}_2 > 2c_1 v \sigma_2, & \text{for B-G case.}
\end{cases}
\tag{64}
$$

In the G interval, $0 < \sigma_1 < v$, $0 < \sigma_2 < v$, and $0 < v < v(t_1)$, which results in $\dot{\sigma}_1 > 0$ and $\dot{\sigma}_2 < 0$ for P-G case, whereas $\dot{\sigma}_1 < 0$ and $\dot{\sigma}_2 > 0$ for B-G case. The P-G sequence is followed by the B interval if $\sigma_2 < 0$ due to negative σ_2 dynamics; the P-G-B solution is feasible, whereas the P-G-P and P-G-C solutions are infeasible. Note that negative σ_2 dynamics in the B interval after the G interval guarantees $\sigma_2 < 0$, i.e., $\sigma_1 > v$, and thus, it cannot generate other intervals. On the other hand, the B-G sequence is followed by the P interval if $\sigma_1 < 0$ due to negative σ_1 dynamics; the B-G-P solution is feasible, whereas the B-G-B solution is infeasible. Note that negative σ_1 dynamics in the P interval after the G interval cannot generate other intervals. Furthermore, the C interval cannot exist after the B-G control sequence because it requires the condition of

$$
\lambda_{1.0} = -3c_1 v_s^2
\tag{65}
$$

and this condition cannot be compatible with the inequality constraint in (63); thus, B-G-C, B-G-C-G, and B-G-C-P solutions are infeasible.

APPENDIX C
FEASIBLE P-C-G-B AND G-C-G-B SOLUTIONS

Three-interval solutions, including the C interval, require the condition in (65). In the same way before, we get the σ dynamics in the last interval of P-C-G, G-C-G, P-C-P, and G-C-P solutions

$$
\begin{cases}
\dot{\sigma}_1 = 2c_1 v \sigma_1 + 3c_1\big(v_s^2 - v^2\big) \\
\dot{\sigma}_2 = 2c_1\big(v\sigma_2 - v_s^2\big) + u_t^* - c_1 v_s^2 - c_0.
\end{cases}
\tag{66}
$$

As for P-C-P and G-C-P solutions, $u_t^* = \bar{u}_t$, $\sigma_1 < 0$, $\sigma_2 > v$, and $v > v_s$ in the last P interval, which results in $\dot{\sigma}_1 < 0$ and $\dot{\sigma}_2 > 0$. The negative σ_1 dynamics in the P interval cannot generate other intervals as same in the B-G-P solution. As for P-C-G and G-C-G solutions, on the other hand, $u_t^* = 0$, $0 < \sigma_1 < v$, $0 < \sigma_2 < v$, and $v < v_s$ in the last G interval, which results in $\dot{\sigma}_1 > 0$ and $\dot{\sigma}_2 < 0$. The negative σ_2 dynamics can generate the B interval if $\sigma_2 < 0$; the P-C-G-B and G-C-G-B solutions are feasible. Note that the negative σ_2 dynamics in the B interval after the G interval cannot generate other intervals as same in the P-G-B solution.

APPENDIX D
EXPLICIT SOLUTION

If x dynamics is the first-order nonlinear ODE of the form $\dot{x} = m(x)n(t)$, its explicit solution form is $\int (dx)/(m(x)) = \int n(t)dt + C$. Moreover, if x dynamics is the first-order linear ODE of the form $\dot{x} + o(t)x = p(t)$, its explicit solution form is $x(t) = [\int p(t)\phi(t)dt + C]/\phi(t)$, where $\phi(t) = e^{\int o(t)dt}$, using the integrating factor method.

Let us define the interval name as $n \in \{P, G, B\}$. If $n = P, G, B$, $u^* = \bar{u}_t, 0, -\bar{u}_b$, and $u^* = \bar{u}_t, 0, -\bar{u}_b$, where $u^* > c_0$ for intervals. For each interval, u^* is constant. The first form can be applied for the v dynamics in (23), and thus, we can get the explicit v solution[5] (V) for the given v_0 and n as follows:

$$
V(t|v_0, n) =
\begin{cases}
k_2\left(1 - \dfrac{2}{k_3 e^{2k_1^2 k_2 t} + 1}\right), & n = P \\
k_4 \tan\big(k_5 - k_1^2 k_4 t\big), & n = G \text{ or } B
\end{cases}
\tag{67}
$$

where $k_1 = (c_1)^{1/2}$, $k_2 = (u^* - c_0)^{1/2}/k_1$, $k_3 = (k_2 + v_0)/(k_2 - v_0)$, $k_4 = (-(u^* - c_0))^{1/2}/k_1$, and $k_5 = \tan^{-1}(v_0/k_4)$. As $s(t) = \int v(t)dt + s_0$, the explicit s solution (S) with $s_0 = 0$ is

$$
S(t|v_0, n)
$$
$$
=
\begin{cases}
k_2\left(-t + \dfrac{\ln\big(k_3 e^{2k_1^2 k_2 t} + 1\big) - \ln(k_3 + 1)}{k_1^2 k_2}\right), & n = P \\[2mm]
\dfrac{1}{k_1^2} \ln\left(\dfrac{\cos\big(k_5 - k_1^2 k_4 t\big)}{\cos(k_5)}\right), & n = G \text{ or } B.
\end{cases}
\tag{68}
$$

Applying the second form for the σ_1 dynamics in (23), $\sigma_1(t) = [-\int(\lambda_{1.0} + 3k_1^2 v^2(t))\phi(t)dt + C]/\phi(t)$, where $\phi(t) = e^{-2k_1^2 s(t)}$. Using the explicit s and v solutions, we can finally get the explicit σ_1 solution (O) for the given $\sigma_{1.0}$, v_0, and n. The solution is complex, so it is omitted in this article.

APPENDIX E
SOLUTIONS AS A FUNCTION OF SWITCHING SPEEDS

Explicit solutions are rewritten as a function of switching speed, not switching times

$$
V^{-1}(v_i|v_{i-1}, n_i)
$$
$$
=
\begin{cases}
\dfrac{1}{2k_1^2 k_2} \ln\left(\dfrac{(k_2 + v_i)(k_2 - v_{i-1})}{(k_2 + v_{i-1})(k_2 - v_i)}\right), & n_i = P \\[2mm]
\dfrac{1}{k_1^2 k_4}\big(\tan^{-1}(v_{i-1}/k_4) - \tan^{-1}(v_i/k_4)\big), & n_i = G \text{ or } B
\end{cases}
\tag{69}
$$

$$
S(v_i|v_{i-1}, n_i)
$$
$$
=
\begin{cases}
\dfrac{1}{2k_1^2} \ln\left(\dfrac{k_2^2 - v_{i-1}^2}{k_2^2 - v_i^2}\right), & n_i = P \\[2mm]
\dfrac{1}{2k_1^2} \ln\left(\dfrac{k_4^2 + v_{i-1}^2}{k_4^2 + v_i^2}\right), & n_i = G \text{ or } B
\end{cases}
\tag{70}
$$

$$
O(v_i|\sigma_{1.i-1}, v_{i-1}, n_i)
$$
$$
=
\begin{cases}
\dfrac{\sigma_{1.i-1} k_1^2\big(k_2^2 - v_{i-1}^2\big) + k_1^2\big(v_{i-1}^3 - v_i^3\big) + \lambda_{1.0}(v_{i-1} - v_i)}{k_1^2\big(k_2^2 - v_i^2\big)} \\[2mm]
\hspace{4cm} n_i = P \\[2mm]
\dfrac{\sigma_{1.i-1} k_1^2\big(k_4^2 + v_{i-1}^2\big) + k_1^2\big(v_i^3 - v_{i-1}^3\big) + \lambda_{1.0}(v_i - v_{i-1})}{k_1^2\big(k_4^2 + v_i^2\big)} \\[2mm]
\hspace{4cm} n_i = G \text{ or } B.
\end{cases}
\tag{71}
$$

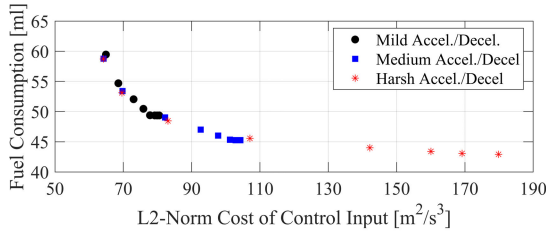[5] For the case where $u^* = c_0$, $V(t|v_0, n) = (v_0)/(1 + v_0 c_1 t)$.

Fig. 14. Tradeoff between fuel consumption and the $L2$-norm cost of control input (i.e., driving comforts).
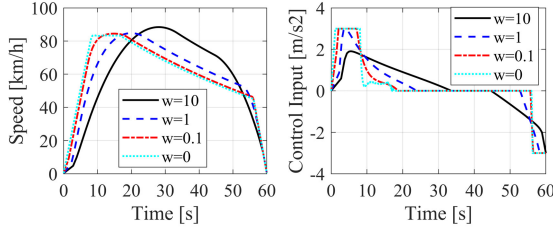

Fig. 15. Speed (left) and control input (right) trajectories depending on different weighting factors with medium acceleration/deceleration limits.

If the $(i-1)$th interval is the C interval, we can use $\sigma_{1.i-1} = 0$ and $\lambda_{1.0} = -3k_1^2 v_{i-1}^2$ to simplify O as follows:

$$O(v_i | \sigma_{1.i-1}, v_{i-1}, n_i)$$
$$= \begin{cases} \dfrac{-2k_1^2 v_{i-1}^3 - k_1^2 v_i^3 + 3k_1^2 v_{i-1}^2 v_i}{k_1^2(k_2^2 - v_i^2)}, & n_i = \mathrm{P} \\ \dfrac{2k_1^2 v_{i-1}^3 + k_1^2 v_i^3 - 3k_1^2 v_{i-1}^2 v_i}{k_1^2(k_4^2 + v_i^2)}, & n_i = \mathrm{G} \end{cases} \tag{72}$$

where the B interval cannot be generated after the C interval.

Appendix F
Driving Comfort's Impact on Fuel-Optimal Driving

To include driving comforts, we define a weighted cost function that includes the $L2$-norm of control input as follows:

$$l = c_1 v^3 + u_b v + w(u_t^2 + u_b^2) \tag{73}$$

where w is a weighting factor. In this study, we consider single-vehicle scenarios with a final time of 60 s. To solve the fuel-optimal OCP with the weighted cost function, we use the direct NLP solver with a grid size of 500. Fig. 14 shows the relationship between $L2$-norm cost and fuel consumption, with three different levels of acceleration/deceleration limits as well as eight different values of the weighting factor. There is a clear tradeoff between driving comforts and fuel savings. Penalizing control inputs in the $L2$ sense (i.e., focusing more on driving comforts) increases fuel consumption. In Fig. 15, we show that the trajectories can be smoothed, especially in the acceleration and braking regimes, but this comes at the cost of increased fuel consumption. Shortening the periods of P, G, and B intervals leads to the increased fuel consumption.

References

[1] J. Rios-Torres and A. A. Malikopoulos, "A survey on the coordination of connected and automated vehicles at intersections and merging at highway on-ramps," *IEEE Trans. Intell. Transp. Syst.*, vol. 18, no. 5, pp. 1066–1077, May 2017.

[2] J. Guanetti, Y. Kim, and F. Borrelli, "Control of connected and automated vehicles: State of the art and future challenges," *Annu. Rev. Control*, vol. 45, pp. 18–40, Jan. 2018.

[3] B. Othman, G. De Nunzio, D. Di Domenico, and C. Canudas-De-Wit, "Ecological traffic management: A review of the modeling and control strategies for improving environmental sustainability of road transportation," *Annu. Rev. Control*, vol. 48, pp. 292–311, Sep. 2019.

[4] R. A. Dollar and A. Vahidi, "Efficient and collision-free anticipative cruise control in randomly mixed strings," *IEEE Trans. Intell. Vehicles*, vol. 3, no. 4, pp. 439–452, Dec. 2018.

[5] S. Bae, Y. Kim, J. Guanetti, F. Borrelli, and S. Moura, "Design and implementation of ecological adaptive cruise control for autonomous driving with communication to traffic lights," in *Proc. Amer. Control Conf. (ACC)*, Philadelphia, PA, USA, Jul. 2019, pp. 4628–4634.

[6] C. Zhai, F. Luo, Y. Liu, and Z. Chen, "Ecological cooperative look-ahead control for automated vehicles travelling on freeways with varying slopes," *IEEE Trans. Veh. Technol.*, vol. 68, no. 2, pp. 1208–1221, Feb. 2019.

[7] G. Guo and Q. Wang, "Fuel-efficient en route speed planning and tracking control of truck platoons," *IEEE Trans. Intell. Transp. Syst.*, vol. 20, no. 8, pp. 3091–3103, Aug. 2019.

[8] A. Vahidi and A. Sciarretta, "Energy saving potentials of connected and automated vehicles," *Transp. Res. C, Emerg. Technol.*, vol. 95, pp. 822–843, Oct. 2018.

[9] A. V. Rao, "Trajectory optimization: A survey," in *Optimization and Optimal Control in Automotive Systems* (Lecture Notes in Control and Information Sciences), vol. 455, H. Waschl, I. Kolmanovsky, M. Steinbuch, and L. Del Re, Eds. Cham, Switzerland: Springer, 2014, pp. 3–21.

[10] F. Mensing, E. Bideaux, R. Trigui, and H. Tattegrain, "Trajectory optimization for eco-driving taking into account traffic constraints," *Transp. Res. D, Transp. Environ.*, vol. 18, pp. 55–61, Jan. 2013.

[11] D. Maamria, K. Gillet, G. Colin, Y. Chamaillard, and C. Nouillant, "Computation of eco-driving cycles for hybrid electric vehicles: Comparative analysis," *Control Eng. Pract.*, vol. 71, pp. 44–52, Feb. 2018.

[12] X. He, H. X. Liu, and X. Liu, "Optimal vehicle speed trajectory on a signalized arterial with consideration of queue," *Transp. Res. C, Emerg. Technol.*, vol. 61, pp. 106–120, Dec. 2015.

[13] S. van de Hoef, K. H. Johansson, and D. V. Dimarogonas, "Efficient dynamic programming solution to a platoon coordination merge problem with stochastic travel times," *IFAC-PapersOnLine*, vol. 50, no. 1, pp. 4228–4233, Jul. 2017.

[14] X. Zeng and J. Wang, "Globally energy-optimal speed planning for road vehicles on a given route," *Transp. Res. C, Emerg. Technol.*, vol. 93, pp. 148–160, Aug. 2018.

[15] E. Ozatay et al., "Cloud-based velocity profile optimization for everyday driving: A dynamic-programming-based solution," *IEEE Trans. Intell. Transp. Syst.*, vol. 15, no. 6, pp. 2491–2505, Dec. 2014.

[16] S. A. Fayazi and A. Vahidi, "Crowdsourcing phase and timing of pre-timed traffic signals in the presence of queues: Algorithms and back-end system architecture," *IEEE Trans. Intell. Transp. Syst.*, vol. 17, no. 3, pp. 870–881, Mar. 2016.

[17] B. van Arem, C. J. G. van Driel, and R. Visser, "The impact of cooperative adaptive cruise control on traffic-flow characteristics," *IEEE Trans. Intell. Transp. Syst.*, vol. 7, no. 4, pp. 429–436, Dec. 2006.

[18] W. B. Dunbar and D. S. Caveney, "Distributed receding horizon control of vehicle platoons: Stability and string stability," *IEEE Trans. Autom. Control*, vol. 57, no. 3, pp. 620–633, Mar. 2012.

[19] Y. Zhang, Y. Bai, M. Wang, and J. Hu, "Cooperative adaptive cruise control with robustness against communication delay: An approach in the space domain," *IEEE Trans. Intell. Transp. Syst.*, vol. 22, no. 9, pp. 1–12, Apr. 2020.

[20] Q. Jin, G. Wu, K. Boriboonsomsin, and M. J. Barth, "Power-based optimal longitudinal control for a connected eco-driving system," *IEEE Trans. Intell. Transp. Syst.*, vol. 17, no. 10, pp. 2900–2910, Oct. 2016.

[21] C. Zhai, F. Luo, and Y. Liu, "Cooperative look-ahead control of vehicle platoon for maximizing fuel efficiency under system constraints," *IEEE Access*, vol. 6, pp. 37700–37714, 2018.

[22] L. Bittner, L. S. Pontryagin, V. G. Boltyanskii, R. V. Gamkrelidze, and E. F. Mishechenko, "The mathematical theory of optimal processes," in *ZAMM—Zeitschrift Für Angewandte Mathematik Und Mechanik*, vol. 43, nos. 10–11. New York, NY, USA: Wiley, 1963, pp. 514–515.

[23] J. Han, A. Vahidi, and A. Sciarretta, "Fundamentals of energy efficient driving for combustion engine and electric vehicles: An optimal control perspective," *Automatica*, vol. 103, pp. 558–572, May 2019.

[24] Y. Kim, M. Figueroa-Santos, N. Prakash, S. Baek, J. B. Siegel, and D. M. Rizzo, "Co-optimization of speed trajectory and power management for a fuel-cell/battery electric vehicle," *Appl. Energy*, vol. 260, Feb. 2020, Art. no. 114254.

[25] A. Sciarretta, G. De Nunzio, and L. L. Ojeda, "Optimal ecodriving control: Energy-efficient driving of road vehicles as an optimal control problem," *IEEE Control Syst. Mag.*, vol. 35, no. 5, pp. 71–90, Oct. 2015.

[26] G. M. Scheepmaker, R. M. P. Goverde, and L. G. Kroon, "Review of energy-efficient train control and timetabling," *Eur. J. Oper. Res.*, vol. 257, no. 2, pp. 355–376, Mar. 2017.

[27] M. Wang, W. Daamen, S. P. Hoogendoorn, and B. van Arem, "Rolling horizon control framework for driver assistance systems. Part I: Mathematical formulation and non-cooperative systems," *Transp. Res. C, Emerg. Technol.*, vol. 40, pp. 271–289, Mar. 2014.

[28] Y. Chen, N. Rozkvas, and M. Lazar, "Driving mode optimization for hybrid trucks using road and traffic preview data," *Energies*, vol. 13, no. 20, p. 5341, Oct. 2020. [Online]. Available: https://www.mdpi.com/1996-1073/13/20/5341

[29] G. R. G. da Silva and M. Lazar, "Long hauling eco-driving: Heavy-duty trucks operational modes control with integrated road slope preview," 2022, *arXiv:2203.12378*.

[30] N. Wan, A. Vahidi, and A. Luckow, "Optimal speed advisory for connected vehicles in arterial roads and the impact on mixed traffic," *Transp. Res. C, Emerg. Technol.*, vol. 69, pp. 548–563, Aug. 2016.

[31] E. Ozatay, U. Ozguner, and D. Filev, "Velocity profile optimization of on road vehicles: Pontryagin's maximum principle based approach," *Control Eng. Pract.*, vol. 61, pp. 244–254, Apr. 2017.

[32] J. Han, A. Sciarretta, L. L. Ojeda, G. De Nunzio, and L. Thibault, "Safe- and eco-driving control for connected and automated electric vehicles using analytical state-constrained optimal solution," *IEEE Trans. Intell. Vehicles*, vol. 3, no. 2, pp. 163–172, Jun. 2018.

[33] A. A. Malikopoulos, C. G. Cassandras, and Y. J. Zhang, "A decentralized energy-optimal control framework for connected automated vehicles at signal-free intersections," *Automatica*, vol. 93, pp. 244–256, Jul. 2018.

[34] A. A. Malikopoulos and L. Zhao, "A closed-form analytical solution for optimal coordination of connected and automated vehicles," in *Proc. Amer. Control Conf. (ACC)*, Philadelphia, PA, USA, Jul. 2019, pp. 3599–3604.

[35] J. Han, D. Karbowski, and N. Kim, "Closed-form solutions for a real-time energy-optimal and collision-free speed planner with limited information," in *Proc. Amer. Control Conf. (ACC)*, Denver, CO, USA, Jul. 2020, pp. 268–275.

[36] T. Ohtsuka, "A continuation/GMRES method for fast computation of nonlinear receding horizon control," *Automatica*, vol. 40, no. 4, pp. 563–574, Apr. 2004.

[37] H. Abbas, Y. Kim, J. B. Siegel, and D. M. Rizzo, "Synthesis of Pontryagin's maximum principle analysis for speed profile optimization of all-electric vehicles," *J. Dyn. Syst., Meas., Control*, vol. 141, no. 7, Jul. 2019, Art. no. 071004.

[38] S. E. Li and H. Peng, "Strategies to minimize the fuel consumption of passenger cars during car-following scenarios," *Proc. Inst. Mech. Eng., D, J. Automobile Eng.*, vol. 226, no. 3, pp. 419–429, Mar. 2012.

[39] D. Shen, D. Karbowski, and A. Rousseau, "Fuel-optimal periodic control of passenger cars in cruise based on Pontryagin's minimum principle," *IFAC-PapersOnLine*, vol. 51, no. 31, pp. 813–820, 2018.

[40] J. Rios-Torres, J. Han, R. Arvin, and A. Khattak, "Automated vehicles merging at highway on-ramps enhanced by connectivity with infrastructure: Safety, mobility, and fuel consumption impacts," presented at the 99th Annu. Meeting Transp. Res. Board, 2020. [Online]. Available: https://annualmeeting.mytrb.org/OnlineProgramArchive/Details/14078

[41] M. A. S. Kamal, M. Mukai, J. Murata, and T. Kawabe, "Ecological vehicle control on roads with up-down slopes," *IEEE Trans. Intell. Transp. Syst.*, vol. 12, no. 3, pp. 783–794, Sep. 2011.

[42] C. R. He, H. Maurer, and G. Orosz, "Fuel consumption optimization of heavy-duty vehicles with grade, wind, and traffic information," *J. Comput. Nonlinear Dyn.*, vol. 11, no. 6, Nov. 2016.

[43] J. Han, J. Rios-Torres, A. Vahidi, and A. Sciarretta, "Impact of model simplification on optimal control of combustion engine and electric vehicles considering control input constraints," in *Proc. IEEE Vehicle Power Propuls. Conf. (VPPC)*, Aug. 2018, pp. 1–6.

[44] A. Kesting, M. Treiber, and D. Helbing, "Enhanced intelligent driver model to access the impact of driving strategies on traffic capacity," *Phil. Trans. Roy. Soc. A, Math., Phys. Eng. Sci.*, vol. 368, no. 1928, pp. 4585–4605, Oct. 2010.

[45] R. F. Hartl, S. P. Sethi, and R. G. Vickson, "A survey of the maximum principles for optimal control problems with state constraints," *SIAM Rev.*, vol. 37, no. 2, pp. 181–218, Jun. 1995.

Jihun Han received the B.Sc., M.Sc., and Ph.D. degrees in mechanical engineering from the Korea Advanced Institute of Science and Technology (KAIST), Daejeon, South Korea, in 2009, 2011, and 2016, respectively.

He was a Post-Doctoral Research Associate at IFP Energies Nouvelles, Rueil-Malmaison, France, from 2016 to 2017, and the Oak Ridge National Laboratory, Oak Ridge, TN, USA, from 2017 to 2018. He is currently a Principal Research Engineer and he has been with the Transportation and Power Systems Division, Argonne National Laboratory, Lemont, IL, USA, since 2018. His research interests include modeling, control, and simulation with an emphasis on intelligent transportation systems, and connected and automated vehicle systems.

Jackeline Rios-Torres (Senior Member, IEEE) received the B.S. degree in electronic engineering from the Universidad del Valle, Cali, Colombia, in 2008, and the Ph.D. degree in automotive engineering from Clemson University, Clemson, SC, USA, in 2015.

She was a Eugene P. Wigner Fellow with the Energy and Transportation Science Division, Oak Ridge National Laboratory, Oak Ridge, TN, USA. She is a GATE Fellow at the Center for Research and Education in Sustainable Vehicle Systems, CU-ICAR, Greenville, SC, USA. Her research is focused on connected and automated vehicles, intelligent transportation systems, and modeling and energy management control of hybrid electric vehicles/plug-in hybrid electric vehicles.

Dr. Rios-Torres was a recipient of the Southern Automotive Women Forum Scholarship and the Smith Fellowship at CU-ICAR.